

Zero-Shot Adaptation for mmWave Beam-Tracking on Overhead Messenger Wires through Robust Adversarial Reinforcement Learning

Masao Shinzaki, *Student Member, IEEE*, Yusuke Koda, *Student Member, IEEE*, Koji Yamamoto, *Senior Member, IEEE*, Takayuki Nishio, *Senior Member, IEEE*, Masahiro Morikura, *Member, IEEE*, Yushi Shirato, *Member, IEEE*, Daisei Uchida, *Member, IEEE*, and Naoki Kita, *Member, IEEE*

Abstract—This paper discusses the opportunity of bringing the concept of zero-shot adaptation into learning-based millimeter-wave (mmWave) communication systems, particularly in environments with unstable urban infrastructures. Here, zero-shot adaptation implies that a learning agent adapts to unseen scenarios during training without any adaptive fine-tuning. By considering learning-based beam-tracking of a mmWave node placed on an overhead messenger wire, we first discuss the importance of zero-shot adaptation. More specifically, we confirm that the gap between the values of wire tension and total wire mass in training and test scenarios deteriorates the beam-tracking performance in terms of the received power. Motivated by this discussion, we propose a robust beam-tracking method to adapt to a broad range of test scenarios in a zero-shot manner, i.e., without requiring any retraining to adapt the scenarios. The key idea is to leverage a recent, robust adversarial reinforcement learning technique, where such training and test gaps are regarded as disturbances from adversaries. In our case, a beam-tracking agent performs training competitively bases on an intelligent adversary who causes beam misalignments. Numerical evaluations confirm the feasibility of zero-shot adaptation by showing that the on-wire node achieves feasible beam-tracking performance without any adaptive fine-tuning in unseen scenarios.

Index Terms—mmWave communications, beam-tracking, robust adversarial reinforcement learning, zero-shot adaptation, overhead messenger wire.

I. INTRODUCTION

WIRELESS communication technologies in the fifth-generation (5G) mobile network provide multigigabit-per-second data rates, which fulfill the backhaul rate requirements [1], [2]. A key technology of 5G systems is millimeter-wave (mmWave) communications, which is advantageous because its broad spectrum band increases communication capacity [3]. In contrast to time- and cost-intensive optical fiber deployments, a mmWave wireless backhaul network achieves high flexibility, cost efficiency, and rapid deployment of backhaul connections [1].

To expand their coverage of mmWave wireless backhalls, small cell base stations (SBSs) are densely deployed [4].

Masao Shinzaki, Yusuke Koda, Koji Yamamoto, and Masahiro Morikura are with the Graduate School of Informatics, Kyoto University, Kyoto 6068501 Japan. e-mail: {shinzaki@imc.cce., koda@imc.cce., kyamamoto@morikura@}i.kyoto-u.ac.jp.

Takayuki Nishio is with School of Engineering, Tokyo Institute of Technology, Ookayama, Meguro-ku, Tokyo, 158-0084, Japan, e-mail: nishio@ict.e.titech.ac.jp.

D. Uchida, Y. Shirato, and N. Kita are with the NTT Access Network Service Systems Laboratories, NTT Corporation, Hikarinooka, Yokosuka 2390847 Japan.

However, mmWave wireless backhalls are expected to suffer from space limitations while deploying SBSs for the following two reasons. The first reason is that SBSs require accessibility to electric power and Internet connections to transmit data traffic to gateway base stations (BSs). This accessibility limits the space for deploying SBSs on telephone poles or buildings where electric and Internet infrastructures have already been installed. The second reason is that line-of-sight (LOS) connections are necessary for mmWave communications. To compensate for the large pass loss at mmWave bands, beam-forming is performed to increase the effective antenna gain [5]. The mmWave beams can be blocked by common obstacles in urban environments such as buildings and roadside trees [6], [7]. This blockage severely penalizes a link budget owing to the large diffraction loss of mmWaves [8].

To overcome these limitations, we deploy an SBS on overhead messenger wires near a gateway BS, as illustrated in Fig. 1 [9]. Overhead messenger wires can provide SBSs with both electric power and an Internet connection, which aids in overcoming the aforementioned limitations. However, the wind-forced dynamics of SBSs can induce beam misalignments. To prevent beam misalignments, a deep reinforcement learning (RL)-based beam-tracking method was proposed in [9]. The background pertaining to the use of a deep RL-based beam-tracking method is discussed in detail in the subsequent section.

To achieve RL-based beam-tracking in a real-world setting, we leveraged a policy learned by simulation-based training to overcome the following limitations of real-world training. An approach for beam-tracking in the real world is to leverage a policy learned in the real world, but it is not practical. First, training in the real world is time consuming, resulting in a scarcity of data. Second, we may be required to perform adaptive fine-tuning to combat the time variances of the environments. In particular, the wire tension and the total wire mass are not always constant because of the deterioration of overhead messenger wires and the adhesion of water or snow during rainfall or snowfall, respectively. Hence, as a time-efficient method, we obtained a policy learned by simulating the wire dynamics and mmWave propagation. Moreover, for simulation-based training, we must overcome the gap between the simulation and the real world, resulting in the incorporation of the aforementioned adaptive fine-tuning process to adapt to the real-world setting.

To address these problems, this paper proposes a beam-

tracking method in a zero-shot manner by using robust adversarial RL. By using robust adversarial RL, we can obtain a beam-tracking policy that is robust against the differences between training and test scenarios [10]. In robust adversarial RL methods, a protagonist learns a policy that maximizes the reward from the disturbances of the adversary who is learning to minimize the reward. We leveraged a scenario where the adversary appends additional wind in the training scenario to obtain an efficient beam-tracking policy and demonstrate the feasibility of correcting beam misalignment under different values of wire tension and total wire mass based on training scenarios without adaptive fine-tuning.

The contributions of this work are summarized as follows:

- We discuss the importance of zero-shot adaptation in learning-based mmWave communications systems, which is till now unexplored in the wireless communications research area. Here, zero-shot adaptation implies that a learning agent exhibits feasible performances in test scenarios without any adaptive fine-tuning even when there are gaps between the training and test scenarios. For the discussion, we consider learning-based beam-tracking of a mmWave node placed in an unstable urban infrastructure, which is exemplified by an overhead messenger wire, as illustrated in Fig. 1. Given this scenario, through numerical evaluations, we confirm that the gap between the training and test scenarios in terms of the material characteristics of the places where the SBSs are attached (e.g., wire tension and total wire mass in our scenario) deteriorates the beam-tracking performance. This debunks the importance of the aforementioned zero-shot adaptations to provide reliable mmWave links, and to the best of our knowledge, this perspective has not been provided in the literature.
- We demonstrate the feasibility of zero-shot adaptation of learning-based mmWave beam-tracking in the aforementioned scenarios. The key idea is to leverage robust adversarial RL, wherein a beam-tracking agent is trained competitively corresponding to an intelligent adversary that attempts to cause beam misalignments by yielding additional wind disturbances. Through numerical evaluations, we show that even if the wire tension and total wire mass of the test scenario are different from those of the training scenario, the proposed method avoids a drastic performance loss in terms of received power without incorporating adaptive fine-tuning to the test scenario.

The rest of this paper is organized as follows. In Section II, we summarize related works. In Section III, we formulate a system model as an RL task. In Section V, we explain the adversarial RL algorithm. In Section VI, we perform a simulation evaluation of the proposed beam-tracking policy. Finally, we present our conclusions in Section VII.

II. RELATED WORKS

A comparison between previous works and this study is presented in Table I. To search for a beam direction to maximize the received signal power, radio frequency (RF) and non-RF information-based methods have been proposed.

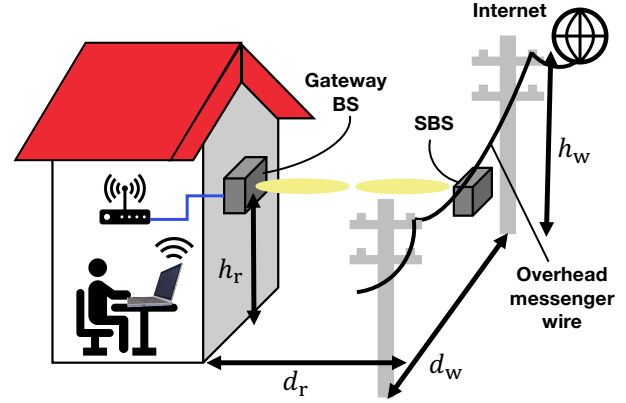


Fig. 1. On-wire SBS in a millimeter-wave backhaul connection.

A. Beam-Tracking with RF Information

To perform beam-tracking, several works focused on RF information, in which several studies have proposed beam-searching methods to shorten the searching time and improve spatial efficiency. This results in reducing the bit error rate and increasing the received signal power by preventing misalignments. In the IEEE 802.11ad standard [27], steering of the transmitter and receiver is decoupled using an omnidirectional antenna. When compared to the exhaustive beam-search scanning of all possible beam directions, an effective approach to search for the optimal beam direction is the process of scanning based on codebooks [11]–[13]. The efficiency of search for the optimal beam direction is enhanced by constructing a hierarchical structure in codebooks [14], [15], or providing the channel state information (CSI) as feedback for codebooks [16], [17].

Recent machine learning (ML) approaches have been used for beam-tracking based on RF information. The beamforming method based on a neural network (NN) proposed in [18] improves robustness to hardware limitations and imperfect CSI for maximizing spectral efficiency. By inputting the channel matrix to the convolutional NN, the latency to select a subarray with optimal spectral efficiency is shortened when compared to optimizing or greedy searching [19], [20]. These beamforming methods based on RF information are not suitable for beamforming of an on-wire SBS because complicated wind-forced dynamics require frequent beam-tracking. Frequent beam-tracking causes large overhead for the beam search, resulting in deterioration of the spectral efficiency. To prevent this problem, we use non-RF information for beam-tracking.

B. Beam-Tracking Based with Non-RF Information

Recent ML approaches have also been used for beam-tracking based on non-RF information. As a type of non-RF information, several works utilized the position of transmitters for the input of ML. In [21], [22], vehicles predicted the optimal power and beam index based on the locations of the receiver and surrounding vehicles. A Q-learning-based algorithm can maximize the received power in a non-LOS scenario [23]. In recent works [24], [25], a deep RL algorithm using position information has been proposed for communication

TABLE I
PREVIOUS WORKS ON BEAM-TRACKING

Reference	Beam-tracking with non-RF	Using ML	Complicated dynamics	Different scenario from training
[11]–[17]	No	No	–	–
[18]–[20]	No	Yes	–	–
[21]–[25]	Yes	Yes	No	No
Previous version [9], [26]	Yes	Yes	Yes	No
This paper	Yes	Yes	Yes	Yes

with mobile objects such as vehicles and user equipment. However, these works assume the simple movement of transmitters or receivers in a test scenario that is similar to the training scenarios.

In our previous works [9], [26], the installation of SBSs on overhead messenger wires was proposed to gain flexibility in physical deployments of SBSs and to ensure LOS connections between SBSs and gateway BSs. These installations pose challenges of beam-tracking because complicated wind-forced dynamics in on-wire SBSs require frequent beam training, and consequently, a large signaling overhead. To address this problem, our previous works demonstrated the feasibility of learning-based beam-tracking using non-RF information.

The difference between this work and our previous works is that the test scenarios are different from the training scenarios in terms of wire tension and total wire mass. Although we considered a specific scenario of overhead messenger wires, the problem caused by the training and test gap itself has not been fully investigated in the literature on the wireless communications research area. Hence, our insights from demonstrating the feasibility of a zero-shot adaptation by robust adversarial RL will highlight a method for overcoming various training-test gaps that arise in learning-based wireless communication systems, such as the gaps between simulation and real-world scenarios and the gaps due to time variances of the wireless environments.

III. SYSTEM MODEL

Fig. 1 shows the system model for an on-wire SBS mmWave backhaul connection. The SBS on the overhead messenger wire communicates with the gateway BS mounted on the building surface through a mmWave link to relay data from the gateway BS to the overhead messenger wire, and vice-versa. In short, the on-wire SBS backhaul provides a connection to the Internet infrastructure directly from an overhead messenger wire near the building.

In this system, the SBS installed on an overhead messenger wire with a weight of m performs beamforming to increase the received signal power of the gateway BS. The endpoints of the overhead messenger wire are fixed to the telephone poles at a height h_w , with a distance d_w between the poles. The gateway BS is mounted at a height h_r , and the distance between the overhead messenger wire and the SBS is d_r in the initial state.

Fig. 2 shows the coordinate system. The origin of the xyz -coordinate system corresponds to the midpoint of the overhead messenger wire. The x -axis corresponds to the line between the endpoints and the z -axis is perpendicular to the ground.

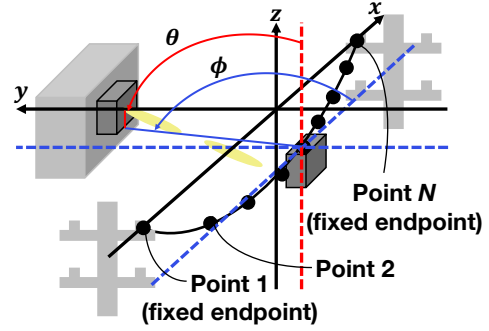


Fig. 2. Coordinate system of the system model.

In Fig. 2, the zenith angle θ and azimuth angle ϕ from the SBS are depicted; they are given by $\theta \in [0^\circ, 180^\circ]$ and $\phi \in [0^\circ, 360^\circ]$, respectively.

A. Model of Dynamics in Overhead Messenger Wire

The overhead messenger wire is modeled as N mass points with a weight of m/N connected by springs with the same spring constant k_0 [28]. Note that the spring constant represents the wire tension. For $i = 1, 2, \dots, N$, the i th point from one end of the overhead messenger wire is called point i . The term $\mathbf{a}_i(t) \in \mathbb{R}^3$ denotes the acceleration of point i at time t . The accelerations of points 1 and N fixed to the telephone poles are expressed as $\mathbf{a}_1(t) = \mathbf{a}_N(t) = \mathbf{0}$. For $i = 2, 3, \dots, N-1$, from the equation of motion, $\mathbf{a}_i(t)$ is given by

$$\mathbf{a}_i(t) = \mathbf{g} + \underbrace{\frac{k_0 N}{m} [\mathbf{x}_{i+1}(t) + \mathbf{x}_{i-1}(t) - 2\mathbf{x}_i(t)]}_{\text{acceleration from tensile force}}, \quad (1)$$

where $\mathbf{x}_i(t) \in \mathbb{R}^3$, $\mathbf{g} \in \mathbb{R}^3$, and k_0 denote the position of point i at time t , gravitational acceleration, and spring constant of the overhead messenger wire, respectively.

The wind drag primarily consists of frictional drag and pressure drag [29]. The frictional drag increases as the wind speed increases, while the pressure drag is a random magnitude regardless of the wind speed. The derivatives of the position and velocity of point i at time t are denoted by $d\mathbf{v}_i(t) \in \mathbb{R}^3$ and $d\mathbf{r}_i(t) \in \mathbb{R}^3$, respectively. The derivatives of the positions and velocities of points 1 and N are expressed as $d\mathbf{v}_1(t) = d\mathbf{v}_N(t) = d\mathbf{x}_1(t) = d\mathbf{x}_N(t) = \mathbf{0}$, respectively. For

$i = 2, 3, \dots, N-1$, $d\mathbf{v}_i(t)$ and $d\mathbf{r}_i(t)$ are calculated as follows [30], [31]:

$$\begin{aligned} d\mathbf{v}_i(t) &= \mathbf{a}_i(t) dt - c_0 \underbrace{[\mathbf{v}_i(t) - \mathbf{v}_0(t)] dt + \mathbf{V}_0 d\mathbf{W}_i(t)}_{\text{derivatives from the wind}}, \\ d\mathbf{r}_i(t) &= \mathbf{v}_i(t) dt, \end{aligned} \quad (2)$$

where c_0 and $\mathbf{v}_0(t) \in \mathbb{R}^3$ denote the drag constant and wind speed, respectively. Moreover, $\mathbf{V}_0 \in \mathbb{R}^{3 \times 3}$ and $\mathbf{W}_i(t) \in \mathbb{R}^3$ denote the covariance matrix of the wind speed and the standard Wiener process that is independently and identically distributed across positions of point i , respectively.

B. Radio-Wave Propagation Model

According to the free space path loss model [32], we consider that the received signal power of the gateway BS $P_r(d, \theta, \phi, \theta_s, \phi_s)$ is determined by the distance d between the SBS and the gateway BS and the antenna radiation pattern. Note that we considered the use of a directional antenna; hence, the antenna radiation pattern is determined by the beam zenith and azimuth angles from the SBS to the gateway BS, i.e., θ, ϕ , respectively, and the zenith and azimuth steering angles, i.e., θ_s, ϕ_s , respectively. From the Friis transmission equation [32], $P_r(d, \theta, \phi, \theta_s, \phi_s)$ is given by

$$P_r(d, \theta, \phi, \theta_s, \phi_s) = \left(\frac{\lambda}{4\pi d} \right)^2 A_t(\theta, \phi, \theta_s, \phi_s) A_r P_t, \quad (3)$$

where P_t , λ , and A_r are constants, and denote the transmission power of the SBS, radio-wave wavelength, and receiver antenna gain, respectively. Moreover, $A_t(\theta, \phi, \theta_s, \phi_s)$ denotes the transmission antenna gain, with its maximum value at $\theta = \theta_s$ and $\phi = \phi_s$. We considered the use of an array antenna; hence, the transmission antenna gain $A_t(\theta, \phi, \theta_s, \phi_s)$ is given by [33], [34]

$$A_t(\theta, \phi, \theta_s, \phi_s) = A_E(\theta, \phi) + AF(\theta, \phi, \theta_s, \phi_s), \quad (4)$$

where $A_E(\theta, \phi)$ and $AF(\theta, \phi, \theta_s, \phi_s)$ denote the element radiation pattern and array factor, respectively.

The third-generation partnership project element radiation pattern $A_E(\theta, \phi)$ of each single antenna element is composed of horizontal and vertical radiation patterns. The element radiation pattern $A_E(\theta, \phi)$ is given by

$$A_E(\theta, \phi) = G_{\max} - \min \left\{ -[A_{E,V}(\theta) + A_{E,H}(\phi)], A_m \right\}, \quad (5)$$

where $A_{E,V}(\theta)$, $A_{E,H}(\phi)$, G_{\max} , and A_m denote the vertical radiation pattern, horizontal radiation pattern, maximum directional gain of the antenna element, and front-back ratio, respectively. The vertical radiation pattern $A_{E,V}(\theta)$ and the horizontal radiation pattern $A_{E,H}(\phi)$ are obtained as follows:

$$\begin{aligned} A_{E,V}(\theta) &= -\min \left\{ 12 \left(\frac{\theta - 90^\circ}{\theta_{3\text{dB}}} \right)^2, SLA_V \right\}, \\ A_{E,H}(\phi) &= -\min \left\{ 12 \left(\frac{\phi}{\phi_{3\text{dB}}} \right)^2, A_m \right\}, \end{aligned} \quad (6)$$

where $\theta_{3\text{dB}}$, $\phi_{3\text{dB}}$, and SLA_V are the vertical 3 dB beamwidth, horizontal 3 dB beamwidth, and side-lobe level limit, respectively.

The array factor $AF(\theta, \phi, \theta_s, \phi_s)$ models the directivity of an antenna array, which is expressed for an array of $n = n_V n_H$ elements as

$$AF(\theta, \phi, \theta_s, \phi_s) = 10 \log_{10} \left[1 + \rho \left(|\mathbf{a} \cdot \mathbf{w}^T|^2 - 1 \right) \right], \quad (7)$$

where n_V , n_H , and ρ denote the number of vertical elements, number of horizontal elements, and correlation coefficient, respectively. Moreover, $\mathbf{a} \in \mathbb{C}^n$ and $\mathbf{w} \in \mathbb{C}^n$ denote the amplitude and beamforming vectors, respectively. The beamforming vector \mathbf{w} is given by

$$\begin{aligned} \mathbf{w} &= [w_{1,1}, w_{1,2}, \dots, w_{n_V, n_H}], \\ w_{p,r} &= e^{j2\pi[(p-1)\Delta_V \Psi_p / \lambda + (r-1)\Delta_H \Psi_r] / \lambda}, \\ \Psi_p &= \cos \theta - \cos \theta_s, \\ \Psi_r &= \sin \theta \sin \phi - \sin \theta_s \sin \phi_s, \end{aligned} \quad (8)$$

where Δ_V and Δ_H denote the spacing distances between the vertical and horizontal elements of the array, respectively.

The SBS observes the instantaneous received signal power for time T . We assume that the position/velocity of the SBS installed at point $i \in \{1, 2, \dots, N\}$ is observable at intervals of τ . The steering angle can be moved up, down, left, or right by an angle β at intervals of τ .

C. Formulation

For $\mathcal{N} = \{1, 2, \dots, T/\tau\}$, the optimization problem can be formulated as follows:

$$\begin{aligned} &\underset{(a_\theta^{(t)}, a_\phi^{(t)})_{t \in \mathcal{N}}}{\text{maximize}} && \frac{1}{T/\tau} \sum_{t \in \mathcal{N}} P_r^{(t)} \left(d^{(t)}, \theta^{(t)}, \phi^{(t)}, \theta_s^{(t)}, \phi_s^{(t)} \right). \\ &\text{subject to} && d^{(t)} = \|\mathbf{x}_S^{(t)} - \mathbf{x}_G\|, \\ & && \theta^{(t)} = \arccos \frac{x_{S,z}^{(t)} - x_{G,z}}{d^{(t)}}, \\ & && \phi^{(t)} = \arctan \frac{x_{S,y}^{(t)} - x_{G,y}}{x_{S,x}^{(t)} - x_{G,x}}, \\ & && \theta_s^{(t)} = \theta_s^{(t-\tau)} + a_\theta^{(t)} \beta, \\ & && \phi_s^{(t)} = \phi_s^{(t-\tau)} + a_\phi^{(t)} \beta, \\ & && a_\theta^{(t)}, a_\phi^{(t)} \in \{-1, 0, 1\}, \\ & && |a_\theta^{(t)}| + |a_\phi^{(t)}| \leq 1, \end{aligned}$$

where $a_\theta^{(t)}$ and $a_\phi^{(t)}$ denote the action for the zenith and azimuth angles at time step t , respectively, which can move the zenith and azimuth steering angles $\theta_s^{(t)}, \phi_s^{(t)}$ by angle β , respectively. Moreover, $d^{(t)}$, $\theta^{(t)}$, and $\phi^{(t)}$ denote the distance, beam zenith, and azimuth angle from the SBS to the gateway BS at time step t , respectively, which are defined by the positions of the SBS and gateway BS, i.e., $\mathbf{x}_S^{(t)} = [x_{S,x}^{(t)}, x_{S,y}^{(t)}, x_{S,z}^{(t)}] \in \mathbb{R}^3$, $\mathbf{x}_G = [x_{G,x}, x_{G,y}, x_{G,z}] \in \mathbb{R}^3$, respectively.

IV. MOTIVATION OF ZERO-SHOT ADAPTATION

In this section, we discuss the importance of addressing the gap between training and test scenarios in learning-based mmWave beam-tracking, which was previously proposed in [9], [26]. Specifically, through numerical evaluations, we show that an increased gap between training and test scenarios deteriorates the received power in the learning-based beam-tracking. This motivated us to propose the concept of zero-shot adaptation as discussed in Section I; we subsequently discuss the advantage of the zero-shot adaptation.

A. Disadvantage without Zero-Shot Adaptation

We evaluated the received signal power when there is a gap in several environmental parameters between the training and test scenarios. The numerical evaluation of learning-based beam-tracking in [9], [26], which is subject to training and test gaps pertaining to the spring constant and total wire mass using the beam-tracking method proposed in [9], is shown in Fig. 3, where the cross mark represents the spring constant and total wire mass in the training. In Fig. 3, the trained beam-tracking policy is implemented in various settings with different values of the spring constant and total wire mass, which are depicted on the vertical and horizontal axes, respectively. The beam-tracking algorithm and simulation parameters are presented in our previous work [9] and in Section VI, respectively. The average received signal power is sensitive to the differences in the spring constant and total wire mass between the training and test scenarios. This implies that when a gap exists between the training and test scenarios, one cannot necessarily provide a reliable mmWave link with a straightforward application of learning-based beam-tracking.

Based on Fig. 3, we show that smaller values of spring constant and total wire mass tend to decrease the average received signal power. The average received power is sensitive to the spring constant because, based on (1) and (2), it can be noted that a smaller spring constant allows the adjacent points to be more separate, resulting in more violent wire dynamics. Similarly, from (1) and (2), it can be noted that a smaller total wire mass enhances the acceleration, resulting in more violent wire dynamics. Because violent wire dynamics cause rapidly changing SBS dynamics, the SBS is forced to correct beam misalignments frequently. Thus, smaller values of spring constant and total wire mass result in difficulties in achieving a feasible beam-tracking policy.

B. Beam-Tracking Based on Zero-Shot Adaptation

The first advantage of leveraging zero-shot adaptation is to avoid the fine-tuning requirements incurred by the time variance of various environmental parameters (e.g., the spring constant and total wire mass in our case), which is a common solution that is adapted to such time-varying environments. However, incorporating adaptive fine-tuning in another scenario requires time and effort because it is necessary to check the wire condition regularly and collect training data. Moreover, during these maintenance procedures, a shutdown of the backhauling services may be required, which deteriorates the

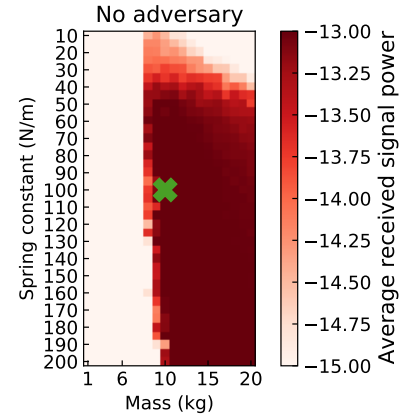


Fig. 3. Heatmap depicting robustness in our previous works based on the spring constant and total wire mass of the messenger wire. The cross mark represents the parameter of the spring constant and total wire mass that was considered during training.

user experience. With zero-shot adaptation, the trained beam-tracking policy can be used in various conditions, even if the environmental parameters demonstrate time variance; hence, one can solve the aforementioned issues.

The second advantage of leveraging zero-shot adaptation is to overcome the gap between a simulation and the real world. To train a beam-tracking policy, one may rely on simulations to overcome the scarcity of real-world training data. However, simulations often differ from the real world. In our case of on-wire mmWave backhauling, the models of wind-forced dynamics and the mmWave propagation leveraged in a simulation may be marginally different from practical situations. Moreover, the actual spring constant and total wire mass in the real world may vary from those in the simulation settings because these types of parameters of a previously installed wire may not be measured accurately. By bringing the zero-shot adaptation, one can solve these problems and deploy a beam-tracking policy trained in a simulation in a plug-and-play manner without experiencing the degradation of the received power incurred by the gaps between the simulation and the real world.

V. ADVERSARIAL RL-BASED BEAM-TRACKING BASED ON ZERO-SHOT ADAPTATION

A. Reason for Adversarial RL

Given the importance of the zero-shot adaptation, we propose a robust adversarial RL-based beam-tracking method. The key reason for the usage of the robust adversarial RL is the capability of overcoming the training and test gap by: 1) regarding the gap as the disturbance from an adversarial agent that impedes the legitimate agent; 2) training both adversarial and legitimate agent and thereby letting the legitimate agent experience more severe disturbances.

The explanation more specific to our beam-tracking problem is as follows: By training the adversarial agent to disturb the on-wire SBS with additional winds, the beam-tracking agent experiences more rapid displacements in the on-wire SBS than without such adversarial agents. We hypothesize that

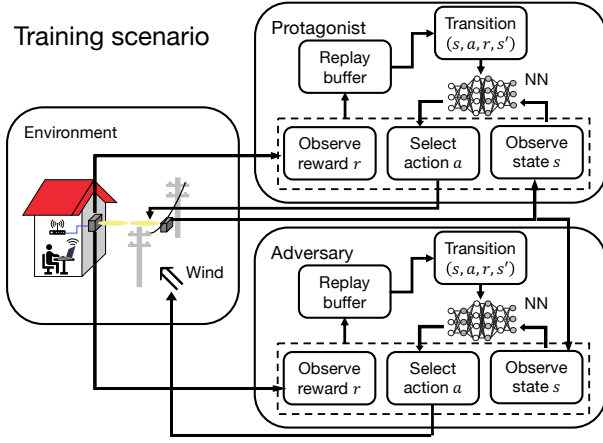


Fig. 4. Training scenario of the adversarial RL.

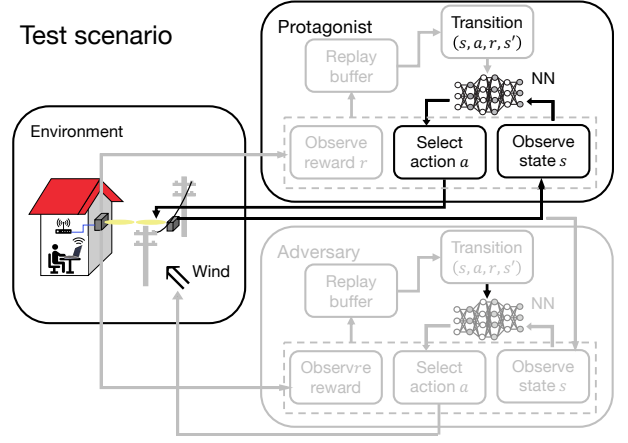


Fig. 5. Test scenario of the adversarial RL.

this well simulates the situation with difficulty in correcting beam-tracking, where the actual wire mass or spring constant is smaller than that in training. This means that the adversarial agent gives richer experiences to the beam-tracking agent in view of the existence of the training and test gap, and hence, we can expect that the beam-tracking agent obtains a robust beam-tracking policy against these training and test gaps.

B. Overview of Adversarial RL-Based Beam-Tracking

The training procedure for adversarial RL-based beam-tracking is shown in Fig. 4. In the training scenario shown in Fig. 4, the protagonist, i.e., the beam-tracking agent, learns to maximize the average received signal power. In contrast, the adversary learns to minimize the average received signal power by blowing an additional wind, which is discussed later. To achieve these purposes, the protagonist and adversary observe a state, select an action, and observe a reward to update their NN from experienced transitions. In the test scenario shown in Fig. 5, the protagonist corrects beam misalignments according to the learned policy in the training scenario. To examine the feasibility of zero-shot adaptation, the environmental parameters, e.g., the spring constant and total wire mass, are varied between the training and test scenarios.

As an example of the disturbance from an adversary, we assume that the adversary can affect the wind speed in the simulation. Thus, the adversary can append discontinuous additional wind to the continuous wind in the environment. At every time step t in the training scenario, by considering the wind speed in the environment $\mathbf{v}_e^{(t)} \in \mathbb{R}^3$ and the additional wind speed appended by the adversary $\mathbf{v}_a^{(t)} \in \mathbb{R}^3$, the wind speed $\mathbf{v}_o^{(t)} \in \mathbb{R}^3$ in (2) is calculated as

$$\mathbf{v}_o^{(t)} = \mathbf{v}_e^{(t)} + \mathbf{v}_a^{(t)}. \quad (9)$$

Conversely, because the adversary does not exist in test scenarios, the wind speed $\mathbf{v}_o^{(t)} \in \mathbb{R}^3$ in (2) is given by

$$\mathbf{v}_o^{(t)} = \mathbf{v}_e^{(t)}. \quad (10)$$

C. State, Action, and Reward

The state set \mathcal{S} of the protagonist and adversary is defined as

$$\mathcal{S} := \mathcal{S}_x \times \mathcal{S}_v \times \mathcal{S}_b, \quad (11)$$

where $\mathcal{S}_x := \{\mathbf{x} \mid \mathbf{x} \in \mathbb{R}^3\}$ and $\mathcal{S}_v := \{\mathbf{v} \mid \mathbf{v} \in \mathbb{R}^3\}$ denote the set of possible three-dimensional positions and velocities of the SBS, respectively. Moreover, $\mathcal{S}_b := \{\mathbf{b} \mid \mathbf{b} \in \mathbb{R}^3\}$ denotes the set of possible beam directions, where beam direction \mathbf{b} is given by

$$\mathbf{b} = [\sin \theta_s \cos \phi_s, \sin \theta_s \sin \phi_s, \cos \theta_s]. \quad (12)$$

Note that these state settings are consistent with our previous works [9], [26] to ensure a fair comparison with these works.

The action set of the protagonist \mathcal{A}_p is defined as

$$\mathcal{A}_p := \{\text{stay, up, down, left, right}\}, \quad (13)$$

where the action stay denotes maintaining the beam direction. Moreover, the actions up, down, left, and right denote moving the beam direction up, down, left, and right by β , respectively. The actions for the zenith and azimuth angle $a_\theta^{(t)}, a_\phi^{(t)}$ are given by

$$\begin{bmatrix} a_\theta^{(t)} \\ a_\phi^{(t)} \end{bmatrix} = \begin{cases} [0, 0], & a_t = \text{stay}; \\ [-1, 0], & a_t = \text{up}; \\ [1, 0], & a_t = \text{down}; \\ [0, 1], & a_t = \text{left}; \\ [0, -1], & a_t = \text{right}. \end{cases} \quad (14)$$

Meanwhile, the action set of the adversary \mathcal{A}_a is defined as

$$\mathcal{A}_a := \{\text{stay, up, down, left, right, front, back}\}, \quad (15)$$

where the action stay denotes that no additional wind is appended. Further, in the training scenarios, the actions up, down, left, right, front, and back denote appending a wind in the upward, downward, leftward, rightward, frontward, and

backward directions with a wind speed of v_a . The additional wind speed by the adversary $v_a^{(t)}$ is given by

$$v_a^{(t)} = \begin{cases} [0, 0, 0], & a_t = \text{stay}; \\ [0, 0, v_a], & a_t = \text{up}; \\ [0, 0, -v_a], & a_t = \text{down}; \\ [-v_a, 0, 0], & a_t = \text{left}; \\ [v_a, 0, 0], & a_t = \text{right}; \\ [0, v_a, 0], & a_t = \text{front}; \\ [0, -v_a, 0], & a_t = \text{back}. \end{cases} \quad (16)$$

The immediate reward is defined as the clipping of the instantaneous received signal power [35]:

$$r_p = \begin{cases} 1, & (P_r - b_c)/d_c > 1; \\ (P_r - b_c)/d_c, & -1 \leq (P_r - b_c)/d_c \leq 1; \\ -1, & (P_r - b_c)/d_c < -1, \end{cases} \quad (17)$$

where P_r denotes the instantaneous received signal power. Moreover, b_c and d_c denote the offset and scale of clipping, respectively. The immediate reward of the adversary r_a is defined as the sign inversion of that of the protagonist. Therefore, the immediate reward of the adversary r_a is given by $r_a = -r_p$.

D. Adversarial RL Algorithm

Algorithm 1 shows an adversarial deep RL-based algorithm used to obtain the beam-tracking policy in the training scenario. For $t = 1, 2, \dots, T/\tau$, the state $s_t \in \mathcal{S}$ is expressed as $s_t = (x_t, v_t, b_t)$. The action a_t is the action selected at time step t , and reward r_t is calculated from (17). In the test scenario, when the state s is observed, the action a that maximizes the predicted discounted reward is selected, which is expressed as $a = \arg \max_{a' \in \mathcal{A}} Q(s, a'; \theta)$.

The purpose of RL is to maximize the discounted reward R_t :

$$R_t = \sum_{\tau=0}^{\infty} \gamma^\tau r_{t+1+\tau}, \quad (18)$$

where r_t and $\gamma \in [0, 1]$ denote the reward obtained at time step t and the discount rate, respectively. The policy $\pi(a | s)$ is the probability of selecting an action $a \in \mathcal{A}$ in state $s \in \mathcal{S}$. The action-value function $Q^\pi(s, a)$ is the expected value of the discounted reward when an action is selected according to the policy $\pi(a | s)$ and is given by

$$Q^\pi(s, a) = \mathbb{E}[R_t | s_t = s, a_t = a, \pi], \quad (19)$$

where $s_t \in \mathcal{S}$ and $a_t \in \mathcal{A}$ denote the state and action at the time step t , respectively. The optimal action-value function $Q^*(s, a)$, where the policy-selected action maximizes the discounted reward, is given by

$$Q^*(s, a) = \max_{\pi} Q^\pi(s, a). \quad (20)$$

The discounted reward can be maximized by selecting an action:

$$a = \arg \max_{a' \in \mathcal{A}} Q^*(s, a'). \quad (21)$$

Algorithm 1 Beam-tracking with Adversarial RL

- 1: Initialize main Q-network and target Q-network of protagonist, i.e., $Q_p(s, a; \theta_p)$ and $Q_p(s, a; \theta_p^-)$, respectively, with random weight θ_{p0} and experience replay buffer of protagonist \mathcal{D}_p
- 2: Initialize main Q-network and target Q-network of adversary, i.e., $Q_a(s, a; \theta_a)$ and $Q_a(s, a; \theta_a^-)$, respectively, with random weight θ_{a0} and experience replay buffer of adversary \mathcal{D}_a
- 3: specify $\epsilon_p, \epsilon_a, \gamma_p, \gamma_a, \alpha_p$ and α_a
- 4: **for** episode $e = 1, 2, \dots, M$ **do**
- 5: Observe position $x_S^{(0)}$, velocity $v_S^{(0)}$, and beam direction $b^{(0)}$
- 6: Select action of protagonist, i.e., stay, up, down, left, or right, randomly
- 7: Select action of adversary, i.e., stay, up, down, left, right, front, or back, randomly
- 8: Observe received signal power $P_t^{(0)}$
- 9: **for** time step $t = 2, \dots, T/\tau$ **do**
- 10: Observe position $x_S^{(t\tau)}$, velocity $v_S^{(t\tau)}$, and beam direction $b_S^{(t\tau)}$
- 11: **if** $\text{rand}(\cdot) < \epsilon$ **then**
- 12: Select action of protagonist, i.e., stay, up, down, left, or right, randomly
- 13: **else**
- 14: Select action of protagonist, i.e., stay, up, down, left, or right, in terms of maximizing the predicted discounted reward.
- 15: **end if**
- 16: **if** $\text{rand}(\cdot) < \epsilon$ **then**
- 17: Select action of adversary, i.e., stay, up, down, left, right, front, or back, randomly
- 18: **else**
- 19: Select action of adversary, i.e., stay, up, down, left, right, front, or back, in terms of maximizing the predicted discounted reward.
- 20: **end if**
- 21: Store transition $(s_{p,t-\tau}, a_{p,t-\tau}, r_{p,t-\tau}, s_{p,t})$ into \mathcal{D}_p
- 22: Store transition $(s_{a,t-\tau}, a_{a,t-\tau}, r_{a,t-\tau}, s_{a,t})$ into \mathcal{D}_a
- 23: Observe received signal power $P_t^{(t)}$
- 24: **end for**
- 25: Update weights of main Q-network of protagonist and adversary θ_p, θ_a by a randomly sampled batch of transitions $\mathcal{B}_p = \{(s, a, r, s')\}$ from \mathcal{D}_p and $\mathcal{B}_a = \{(s, a, r, s')\}$ from \mathcal{D}_a
- 26: **if** $e \equiv 0 \pmod{e_p}$ **then**
- 27: Replace weights of target Q-network $\theta_p^- \leftarrow \theta_p$
- 28: **end if**
- 29: **if** $e \equiv 0 \pmod{e_a}$ **then**
- 30: Replace weights of target Q-network $\theta_a^- \leftarrow \theta_a$
- 31: **end if**
- 32: **end for**

In a deep Q-network (DQN), the action-value function is approximated by a NN. The action-value function approximated by a NN $Q(s, a; \theta)$ is called the Q-network. To obtain a policy to maximize the discounted reward, we improved the accuracy of the approximation by using experience replay [36], double

DQN (DDQN) [37], [38], Huber loss [39], and dueling DQN [40].

The accuracy of the approximation is evaluated by the loss function $L(\theta)$. The approximation of the NN is considered to be more accurate if the loss function, which is positive, exhibits values closer to zero. The weights of θ are updated to improve the accuracy of the approximation of the NN. The loss function $L(\theta)$ is given by

$$L(\theta) = \mathbb{E}_{s,a,r,s'} [\mathcal{L}(e)], \quad (22)$$

where \mathcal{L} and e denote the error function and error, respectively. Moreover, $s' \in \mathcal{S}$ and $a' \in \mathcal{A}$ are the next state and action of $s \in \mathcal{S}$ and $a \in \mathcal{A}$, respectively. The immediate reward r is obtained after performing $a \in \mathcal{A}$. We used Huber loss [39] as it is an error function that is robust to outliers. The Huber loss is given by:

$$\mathcal{L}(x) = \begin{cases} x^2/2, & x \leq 1; \\ |x| - 0.5, & \text{otherwise.} \end{cases} \quad (23)$$

In DQN, the error e is obtained by

$$e = r + \gamma \max_{a'} Q(s', a'; \theta^-) - Q(s, a; \theta_i). \quad (24)$$

In experience replay [36], transitions (s_t, a_t, r_t, s_{t+1}) are stored in a replay buffer \mathcal{D} . A mini-batch \mathcal{B} , randomly created from replay buffer \mathcal{D} , is used for learning.

In DDQN, two Q-networks, i.e., a main Q-network $Q(s, a; \theta)$ and a target Q-network $Q(s, a; \theta^-)$ are used [37], [38]. The learning is more stable by evaluating the error using the target Q-network in which weights are updated to the weights of the main Q-network at every t_u step.

Each Q network is divided into two functions as Dueling DQN [40]. In the dueling DQN, the action-value function $Q^\pi(s, a)$ is divided into a state-value function $V^\pi(s)$ and an advantage function $A^\pi(s, a)$. The state-value and advantage functions are expressed as follows:

$$\begin{aligned} V^\pi(s) &= \mathbb{E}_{a \sim \pi(s)} [Q^\pi(s, a)], \\ A^\pi(s, a) &= Q^\pi(s, a) - V^\pi(s). \end{aligned} \quad (25)$$

By using the state-value function approximated by NN $V(s; \theta_V)$ and the advantage function approximated by NN $A(s, a; \theta_A)$, the Q-network $Q(s, a; \theta^-)$ is expressed as follows:

$$\begin{aligned} Q(s, a; \theta) &= V(s; \theta_V) \\ &+ \left(A(s, a; \theta_A) - \frac{1}{|\mathcal{A}|} \sum_{a'} A(s, a'; \theta_A) \right), \end{aligned} \quad (26)$$

where θ_V and θ_A are the weights for approximating the state-value and advantage functions by NN, respectively. Note that $\theta = [\theta_V, \theta_A]$.

For exploration and exploitation, we use the ϵ -greedy policy. Setting the exploration rate as $\epsilon \in [0, 1]$, an action is randomly selected from all actions with a probability of ϵ . An action is selected to maximize the Q-network $Q(s, a; \theta)$ with a probability of $1 - \epsilon$.

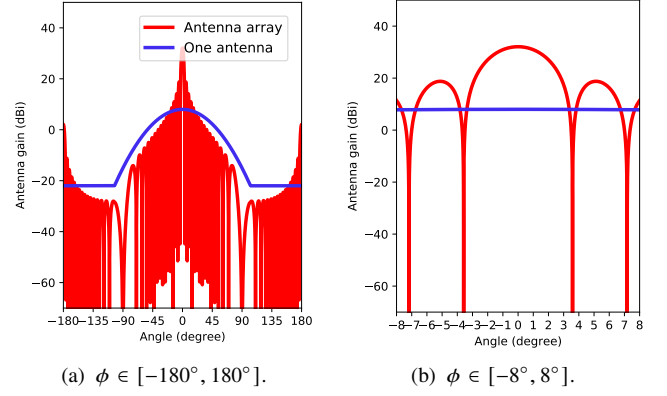


Fig. 6. Antenna pattern. The vertical angle θ was fixed at 90° .

VI. SIMULATION RESULTS

A. Simulation Parameters

The simulation parameters are listed in Table II, where $\mathbf{E} \in \mathbb{R}^{3 \times 3}$ is an identity matrix. The SBS is installed at the midpoint of the overhead messenger wire, which is moved significantly by the wind. The wind speed in the environment $v_e^{(t)}$ is given by

$$v_e^{(t)} = \left[5 \sin \frac{2\pi t}{4}, 5 \sin \frac{2\pi t}{6}, 5 \sin \frac{2\pi t}{8} \right], \quad (27)$$

which follows our previous works [9], [26].

1) *Antenna Pattern*: Fig. 6 shows the antenna pattern based on the simulation parameters listed in Table II. The red line represents the transmission antenna gain with the array factor $AF(\theta, \phi, \theta_s, \phi_s)$. The blue line represents the transmission antenna gain without the array factor, i.e., $AF(\theta, \phi, \theta_s, \phi_s) = 0$ in (4). The directivity of the transmission antenna gain with the array factor is higher than the directivity of the transmission antenna gain without the array factor. In the transmission antenna gain with the array factor, 3.6° is the positive minimum value of the local minimum values.

2) *Architecture of the Neural Network*: We used a NN with three hidden layers, as shown in Fig. 7, where $|\mathcal{A}|$ denotes the number of actions. The number of actions of the protagonist $|\mathcal{A}_p| = 5$ and the number of actions of the adversary $|\mathcal{A}_a| = 7$. The hidden layers were all fully connected and had 32 units. The activation function of the hidden layers was the rectified linear unit $R(x)$ given by

$$R(x) = \max\{x, 0\}. \quad (28)$$

The gradient descent method was Adam [41]; moreover, the learning rates of the protagonist and adversary α_p, α_a were 10^{-3} .

B. Baseline Method

To evaluate the average received signal power of the learned policy of the protagonist, we compared the proposed method with the *stay method* and *upper-limit method*. Because these compared methods aim to evaluate a policy of the protagonist without the disturbances of the adversary, the adversary does not exist in the stay or upper-limit methods. In the stay method,

TABLE II
SIMULATION PARAMETERS

Height of endpoints of wire h_w	5 m
Distance between endpoints d_w	10 m
Height of gateway BS h_r	5 m
Distance between wire and gateway BS d_r	5 m
Transmission power P_t	23 dBm
Radio-wave wavelength λ	5 mm
Receiver antenna gain A_r	8 dBi
Gravitational acceleration g	$[0, 0, -9.8] \text{ ms}^{-2}$
Spring constant k_0	100 Nm^{-1}
Drag constant c_0	1 s^{-1}
Number of points N	11
Total wire mass m	10 kg
Covariance matrix of the wind speed V_0	$0.1E$
Vertical 3 dB beamwidth $\theta_{3\text{dB}}$	65°
Horizontal 3 dB beamwidth $\phi_{3\text{dB}}$	65°
Side-lobe level limit SLA_v	30 dB
Front-back ratio A_m	30 dB
Amplitude vector \mathbf{a}	$[\frac{1}{\sqrt{n}}, \frac{1}{\sqrt{n}}, \dots, \frac{1}{\sqrt{n}}]$
Number of vertical elements n_v	32
Number of horizontal elements n_h	32
Correlation coefficient ρ	1
Zenith steering angle θ_s	90°
Azimuth steering angle ϕ_s	0°
Vertical spacing distance Δv	2.5 mm
Horizontal spacing distance Δh	2.5 mm
Number of episodes M	400
Point of installed SBS	Point 6
Observation time T	10 s
Observation interval τ	0.01 s
Angle when moving beam direction β	1°
Constant in (17) b_c	27
Constant in (17) d_c	3
Exploration rate ϵ_p, ϵ_a	0.2
Discount rate γ_p, γ_a	0.99
Replacing interval in Algorithm 1 e_p, e_a	5
Additional wind speed by the adversary v_a	10 m/s

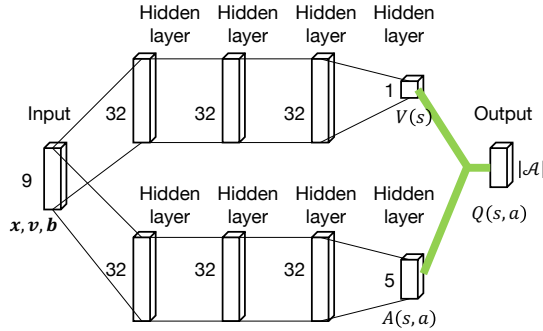


Fig. 7. Architecture of the NN of the protagonist and adversary.

the beam direction is fixed in the initial beam direction. The policy $\pi(a | s)$ of the stay method is given by

$$\pi(a | s) = \begin{cases} 1, & a = \text{stay}; \\ 0, & a = \text{up, down, left, right}. \end{cases} \quad (29)$$

In the upper-limit method, the actions maximize the transmission antenna gain such that a superior performance is exhibited in terms of the received signal power.

To evaluate the robustness of the learned policy of the protagonist, we compared the proposed method with the *no adversary method* and *random 10 m/s method*. In the no adversary method, the policy of the protagonist is learned in

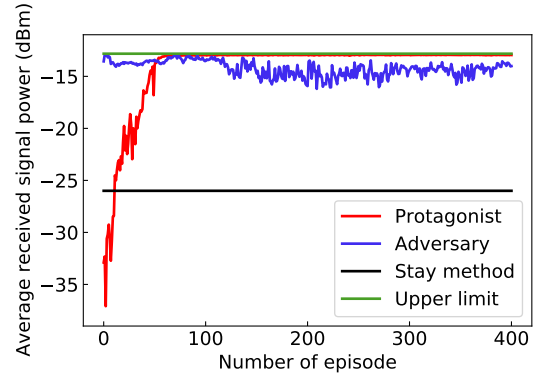


Fig. 8. Learning curve of the protagonist and the adversary. By updating the weights of the NN, the protagonist increases the average received signal power and the adversary decreases the average received signal power.

the scenario where the adversary appends no additional wind, i.e., $v_a = 0$. In the random 10 m/s method, the policy of the protagonist is learned in the scenario where the adversary takes each action at random with equal probability.

C. Learning Curve

To evaluate the effect of the parameter update of the protagonist, the learning curve of the protagonist is shown in Fig. 8. In Fig. 8, the horizontal axis represents the number of episodes and the vertical axis represents the average received signal power of the gateway BS. While considering the learning curve of the protagonist in Fig. 8, it can be noted that the protagonist corrects beam misalignments according to the learned policy, and the adversary appends no additional wind to evaluate the average received signal power of the test scenarios. After the protagonist has learned for 400 episodes, the average received signal power is -12.9 dBm without disturbances from the adversary.

To evaluate the effect of the parameter update of the adversary, the learning curve of the adversary is also shown in Fig. 8. From the learning curve of the adversary in Fig. 8, it can be noted that the protagonist corrects beam misalignments according to a pretrained deep RL method, and the adversary appends additional wind according to the learned policy. After the adversary has learned for 400 episodes, the average received signal power is -14.0 dBm for the pretrained protagonist. Hence, the learned adversary successfully disturbs the pretrained beam-tracking agent.

D. Robustness of the Learned Policy

To demonstrate the robustness to variations in the spring constant, we compared the average received signal power of the proposed method with that of the no adversary and random 10 m/s methods, as shown in Fig. 9. In Fig. 9, the spring constant of the messenger wire is shown in the horizontal axis, where the training parameter of the spring constant is represented by the dashed line. When the spring constant $k_0 = 100 \text{ Nm}^{-1}$, which is the setting in the training, all methods including baseline methods exhibited almost identical received powers, that is, approximately -12.9 dBm . Meanwhile, in the

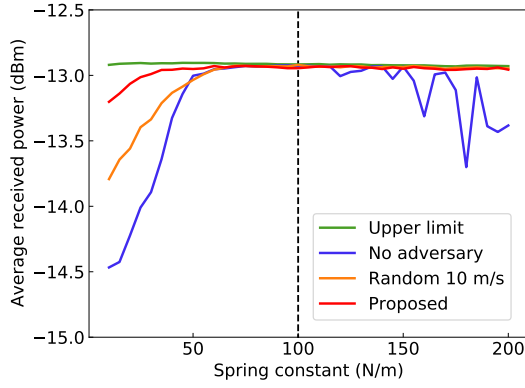


Fig. 9. Robustness to variations in spring constant of the overhead messenger wire. In the test scenarios, the average received signal power of the proposed method is more robust to the different spring constants than the compared methods. The dashed line represents the training parameter of the spring constant.

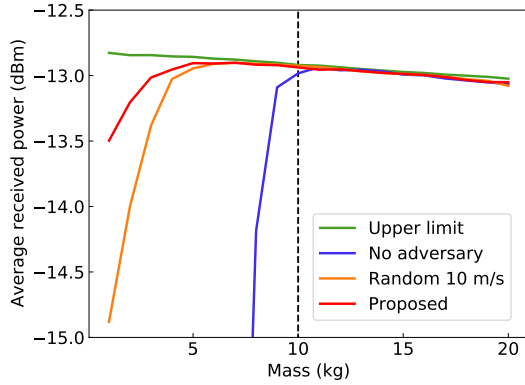


Fig. 10. Robustness to variations in total wire mass. In the test scenarios, the average received signal power of the proposed method is more robust to the various total wire masses than the compared methods. The dashed line represents the training parameter of the total wire mass.

scenario of when the spring constant was lower than that in training, i.e., $k_0 = 10 \text{ Nm}^{-1}$, the average received signal power of the proposed method was -13.2 dBm , while that of the no adversary and random 10 m/s methods dropped to -14.5 and -13.8 dBm , respectively. Note that blowing a random amount of wind is advantageous for the protagonist to learn a robust policy when compared to appending no additional wind. Further, appending an additional wind by the adversary while learning with the protagonist is more effective for the protagonist to learn a robust policy than when a random wind is appended.

To evaluate the robustness to the variations in the total wire mass, we compared the average received signal power of the proposed method with that of the no adversary and random 10 m/s methods, as shown in Fig. 10. In Fig. 10, the total wire mass is shown in the horizontal axis, where the training parameter of the total wire mass is represented by the dashed line, that is, 10 kg . Similar to the results pertaining to the spring constant, the proposed methods exhibited a higher received power for various total wire masses. Hence, the proposed method achieves more robust beam-tracking against

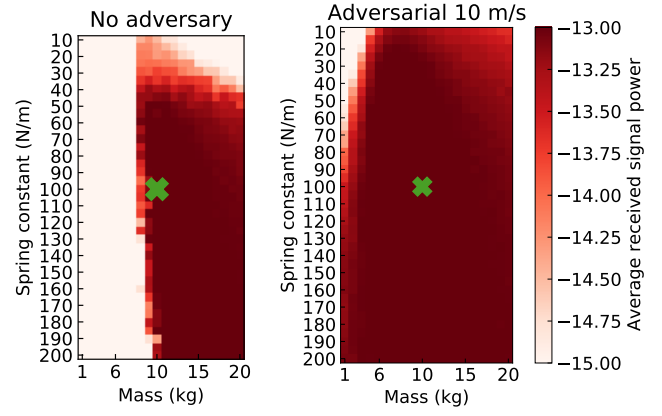


Fig. 11. Heatmap depicting robustness to variations in the spring constant and total wire mass of the messenger wire. In the test scenarios, the average received signal power of the proposed method is more robust to the variations in total wire mass than the no adversary method. The cross mark represents the training parameters of the spring constant and total wire mass.

training and test gaps in terms of total wire masses. Note that this achievement is without any adaptive fine-tuning of the total wire masses and hence demonstrates the feasibility of the aforementioned zero-shot adaptation in mmWave beam-tracking.

To discuss the robustness to varying spring constants and total wire masses, we show the average received signal power for various values of spring constant and total wire mass in Fig. 11. The color of the heatmap represents the average received signal power, where the cross mark represents the training parameters of the spring constant and total wire mass. In Fig. 11, the area of high average received power is shown in red, while that of low average received power is shown in white. Fig. 11 demonstrates that the area of a high average received power of the proposed method is wider than that of the no adversary method. This implies that the proposed method enables the adaptation of various ranges of test settings for beam-tracking without the requirement for adaptive fine-tuning; thus, in this sense, this result demonstrates the feasibility of zero-shot adaptation in learning-based beam-tracking.

VII. CONCLUSION

We discussed the importance of zero-shot adaptation in learning-based mmWave beam-tracking. To demonstrate the feasibility of zero-shot adaptation, we proposed an adversarial RL-based beam-tracking method to obtain a robust beam-tracking policy to overcome the differences between the training and test scenarios, such as the variations in wire tension and the total wire mass. We developed an adversarial RL-based algorithm, where the adversary created an additional wind. We confirmed that in the proposed method, the beam-tracking agent enhanced the average received power and the adversary degraded the average received power. Furthermore, we demonstrated that the proposed method is more robust than not only the no adversary method but also the random 10 m/s method, when assuming an adversary without training. This shows that disturbances of an intelligent adversary increased the robustness of the beam-tracking policy to variations in wire

tension, i.e., the spring constant or total wire mass, which was more than that when the adversary was not trained.

REFERENCES

- [1] Y. Niu, Y. Li, D. Jin, L. Su, and A. V. Vasilakos, "A survey of millimeter wave communications (mmWave) for 5G: Opportunities and challenges," *Wireless netw.*, vol. 21, no. 8, pp. 2657–2676, Nov. 2015.
- [2] S. Rangan, T. S. Rappaport, and E. Erkip, "Millimeter-wave cellular wireless networks: Potentials and challenges," *Proceedings of the IEEE*, vol. 102, no. 3, pp. 366–385, Mar. 2014.
- [3] Q. Cao, H. Rutagemwa, F. Zhou, P. Yu, L. Feng, W. Li, A. Xiong, and X. Qiu, "Capacity enhancement for mmWave multi-beam satellite-terrestrial backhaul via beam sharing," in *Proc. IEEE ICC*. Kansas City, MO, USA: IEEE, May 2018, pp. 1–6.
- [4] L. Zhao, J. Guo, Z. Wei, D. W. K. Ng, and J. Yuan, "A distributed multi-RF chain hybrid mmwave scheme for small-cell systems," in *Proc. IEEE ICC*, Shanghai, China, May 2019, pp. 1–7.
- [5] L. Wei, R. Q. Hu, Y. Qian, and G. Wu, "Key elements to enable millimeter wave communications for 5G wireless systems," *IEEE Wireless Commun.*, vol. 21, no. 6, pp. 136–143, Dec. 2014.
- [6] H. Soleimani, R. Parada, S. Tomasin, and M. Zorzi, "Statistical approaches for initial access in mmwave 5G systems," in *Proc. VOE EW*, Catania, Italy, May 2018, pp. 1–6.
- [7] L. Zhang, X. Chen, Y. Fang, X. Huang, and X. Fang, "Learning-based mmwave V2I environment augmentation through tunable reflectors," in *Proc. IEEE GLOBECOM*, Waikoloa, HI, USA, Dec. 2019, pp. 1–6.
- [8] G. R. MacCartney, S. Deng, S. Sun, and T. S. Rappaport, "Millimeter-wave human blockage at 73 GHz with a simple double knife-edge diffraction model and extension for directional antennas," in *Proc. IEEE VTC-Fall*, Montreal, QC, Canada, Sep. 2016, pp. 1–6.
- [9] M. Shinzaki, Y. Koda, K. Yamamoto, T. Nishio, M. Morikura, H. Chunhsiang, Y. Shirato, and N. Kita, "Deep reinforcement learning-based beam tracking from mmwave antennas installed on overhead messenger wires," in *Proc. IEEE VTC-Fall*, Held Online, Dec. 2020, pp. 1–6.
- [10] L. Pinto, J. Davidson, R. Sukthankar, and A. Gupta, "Robust adversarial reinforcement learning," in *Proc. ICML*, Sydney, Australia, Aug. 2017, pp. 2817–2826.
- [11] V. Raghavan, R. W. Heath, and A. M. Sayeed, "Systematic codebook designs for quantized beamforming in correlated MIMO channels," *IEEE J. Sel. Areas Commun.*, vol. 25, no. 7, pp. 1298–1310, 2007.
- [12] J. Wang, Z. Lan, C.-S. Sum, C.-W. Pyo, J. Gao, T. Baykas, A. Rahman, R. Funada, F. Kojima, I. Lakkis *et al.*, "Beamforming codebook design and performance evaluation for 60 GHz wideband WPANs," in *Proc. IEEE VTC-Fall*, Anchorage, AK, USA, Sep. 2009, pp. 1–6.
- [13] L. Chen, Y. Yang, X. Chen, and W. Wang, "Multi-stage beamforming codebook for 60 GHz WPAN," in *Proc. IEEE CHINACOM*, Harbin, China, Aug. 2011, pp. 361–365.
- [14] J. Wang, Z. Lan, C.-W. Pyo, T. Baykas, C.-S. Sum, M. A. Rahman, J. Gao, R. Funada, F. Kojima, H. Harada *et al.*, "Beam codebook based beamforming protocol for multi-Gbps millimeter-wave WPAN systems," *IEEE J. Sel. Areas Commun.*, vol. 27, no. 8, pp. 1390–1399, Sep. 2009.
- [15] Z. Xiao, T. He, P. Xia, and X.-G. Xia, "Hierarchical codebook design for beamforming training in millimeter-wave communication," *IEEE Trans. Wireless Commun.*, vol. 15, no. 5, pp. 3380–3392, Jan. 2016.
- [16] S. Faxer, S. Bergman, and N. Wernersson, "A codebook-based concept for hybrid CSI feedback in FDD massive MIMO systems," in *Proc. IEEE VTC-Spring*, Nanjing, China, May 2016, pp. 1–6.
- [17] G. Morozov, A. Davydov, and V. Sergeev, "Enhanced CSI feedback for FD-MIMO with beamformed CSI-RS in LTE-A pro systems," in *Proc. IEEE VTC-Fall*, Montreal, QC, Canada, Sep. 2016, pp. 1–5.
- [18] T. Lin and Y. Zhu, "Beamforming design for large-scale antenna arrays using deep learning," *IEEE Wireless Commun. Lett.*, vol. 9, no. 1, pp. 103–107, Sep. 2019.
- [19] A. M. Elbir and K. V. Mishra, "Joint antenna selection and hybrid beamformer design using unquantized and quantized deep learning networks," *IEEE Trans. Wireless Commun.*, vol. 19, no. 3, pp. 1677–1688, Dec. 2019.
- [20] —, "Deep learning design for joint antenna selection and hybrid beamforming in massive MIMO," in *Proc. IEEE ISAP*, Atlanta, GA, USA, Jul. 2019, pp. 1585–1586.
- [21] Y. Wang, M. Narasimha, and R. W. Heath, "Mmwave beam prediction with situational awareness: A machine learning approach," in *Proc. IEEE SPAWC*, Kalamata, Greece, Jun. 2018, pp. 1–5.
- [22] Y. Wang, A. Klautau, M. Ribero, A. C. Soong, and R. W. Heath, "Mmwave vehicular beam selection with situational awareness using machine learning," *IEEE Access*, vol. 7, pp. 87 479–87 493, Jun. 2019.
- [23] R. Wang, O. Onireti, L. Zhang, M. A. Imran, G. Ren, J. Qiu, and T. Tian, "Reinforcement learning method for beam management in millimeter-wave networks," in *Proc. IEEE UCET*, Glasgow, United Kingdom, Aug. 2019, pp. 1–4.
- [24] A. Klautau, P. Batista, N. González-Prelcic, Y. Wang, and R. W. Heath, "5G MIMO data for machine learning: Application to beam-selection using deep learning," in *Proc. IEEE ITA*, San Diego, CA, USA, Feb. 2018, pp. 1–9.
- [25] F. B. Mismar, B. L. Evans, and A. Alkhateeb, "Deep reinforcement learning for 5G networks: Joint beamforming, power control, and interference coordination," *IEEE Trans. Commun.*, vol. 68, no. 3, pp. 1581–1592, Dec. 2019.
- [26] Y. Koda, M. Shinzaki, K. Yamamoto, T. Nishio, M. Morikura, Y. Shirato, D. Uchida, and N. Kita, "Millimeter wave communications on overhead messenger wire: Deep reinforcement learning-based predictive beam tracking," *arXiv preprint arXiv:2012.00982*, 2020.
- [27] "Wireless LAN medium access control (MAC) and physical layer (PHY) specification," IEEE Std. 802.11ad-2012.
- [28] G. M. Gladwell, "Inverse problems in vibration," *Appl. Mech. Rev.*, vol. 39, no. 7, pp. 1013–1018, Jul. 1986.
- [29] M. H. Koo and A. Mahdi, "Calculation of aerodynamic drag of human being in various positions," in *Proc. EURECA*, Kuala Lumpur, Malaysia, Jan. 2013, pp. 99–100.
- [30] R. Zárate-Minano, F. M. Mele, and F. Milano, "SDE-based wind speed models with weibull distribution and exponential autocorrelation," in *Proc. IEEE PESGM*, Boston, MA, USA, Jul. 2016, pp. 1–5.
- [31] H. Shiri, J. Park, and M. Bennis, "Massive autonomous UAV path planning: A neural network based mean-field game theoretic approach," in *Proc. IEEE GLOBECOM*, Honolulu, HI, USA, Dec. 2019, pp. 1–6.
- [32] H. T. Friis, "A note on a simple transmission formula," *Proceedings of the IRE*, vol. 34, no. 5, pp. 254–256, May 1946.
- [33] 3GPP TR 37.840 v12.1.0, "Technical specification group radio access network; study of radio frequency (RF) and electromagnetic compatibility (EMC) requirements for active antenna array system (AAS) base station," Tech. Rep., Dec. 2013.
- [34] M. Rebato, L. Resteghini, C. Mazzucco, and M. Zorzi, "Study of realistic antenna patterns in 5G mmwave cellular scenarios," in *Proc. IEEE ICC*, Kansas City, USA, May 2018, pp. 1–6.
- [35] V. Mnih, K. Kavukcuoglu, D. Silver, A. A. Rusu, J. Veness, M. G. Bellemare *et al.*, "Human-level control through deep reinforcement learning," *Nature*, vol. 518, no. 7540, pp. 529–533, Feb. 2015.
- [36] D. Zhao, H. Wang, K. Shao, and Y. Zhu, "Deep reinforcement learning with experience replay based on SARSA," in *Proc. IEEE SSCI*, Athens, Greece, Dec. 2016, pp. 1–6.
- [37] H. Van Hasselt, A. Guez, and D. Silver, "Deep reinforcement learning with double Q-learning," in *Proc. AAAI*, Phoenix, Arizona, USA, Feb. 2016, pp. 2094–2100.
- [38] Q. Zhang, M. Lin, L. T. Yang, Z. Chen, S. U. Khan, and P. Li, "A double deep Q-learning model for energy-efficient edge scheduling," *IEEE Trans. Serv. Comput.*, vol. 12, no. 5, pp. 739–749, Aug. 2018.
- [39] D. Varga, D. Saupe, and T. Szirányi, "DeepRN: A content preserving deep architecture for blind image quality assessment," in *Proc. IEEE ICME*, San Diego, CA, USA, Jul. 2018, pp. 1–6.
- [40] Z. Wang, T. Schaul, M. Hessel, H. Van Hasselt, M. Lanctot, and N. De Freitas, "Dueling network architectures for deep reinforcement learning," in *Proc. ICML*, New York City, NY, USA, Jun. 2016, pp. 1995–2003.
- [41] D. P. Kingma and J. Ba, "Adam: A method for stochastic optimization," in *In ICLR*, San Diego, CA, USA, May 2015, pp. 1–15.



Masao Shinzaki received the B.E. degree in electrical and electronic engineering from Kyoto University in 2019. He is currently studying toward the M.E. degree at the Graduate School of Informatics from Kyoto University. He is a member of the IEICE.



Yusuke Koda received the B.E. degree in electrical and electronic engineering from Kyoto University in 2016 and the M.E. degree at the Graduate School of Informatics from Kyoto University in 2018. In 2019, he visited Centre for Wireless Communications, University of Oulu, Finland to conduct collaborative research. He is currently studying toward the Ph.D. degree at the Graduate School of Informatics from Kyoto University. He received the VTS Japan Young Researcher's Encouragement Award in 2017 and TELECOM System Technology Award in 2020. He

was a Recipient of the Nokia Foundation Centennial Scholarship in 2019. He is a member of the ACM and IEICE.



Koji Yamamoto (S'03–M'06–SM'20) received the B.E. degree in electrical and electronic engineering from Kyoto University in 2002, and the master and Ph.D. degrees in Informatics from Kyoto University in 2004 and 2005, respectively. From 2004 to 2005, he was a research fellow of the Japan Society for the Promotion of Science (JSPS). Since 2005, he has been with the Graduate School of Informatics, Kyoto University, where he is currently an associate professor. From 2008 to 2009, he was a visiting researcher at Wireless@KTH, Royal Institute of

Technology (KTH) in Sweden. He serves as an editor of IEEE Wireless Communications Letters and Journal of Communications and Information Networks, a track co-chair of APCC 2017, CCNC 2018, APCC 2018, and CCNC 2019, and a vice co-chair of IEEE ComSoc APB CCC. He was a tutorial lecturer in ICC 2019. His research interests include radio resource management, game theory, and machine learning. He received the PIMRC 2004 Best Student Paper Award in 2004, the Ericsson Young Scientist Award in 2006. He also received the Young Researcher's Award, the Paper Award, SUEMATSU-Yasuharu Award from the IEICE of Japan in 2008, 2011, and 2016, respectively, and IEEE Kansai Section GOLD Award in 2012. He is a senior member of the IEICE and a member of the Operations Research Society of Japan.



Takayuki Nishio (S'11–M'14–SM'20) received the B.E. degree in electrical and electronic engineering and the master's and Ph.D. degrees in informatics from Kyoto University in 2010, 2012, and 2013, respectively. He was an assistant professor in communications and computer engineering with the Graduate School of Informatics, Kyoto University from 2013 to 2020. He is currently an associate professor at the School of Engineering, Tokyo Institute of Technology, Japan. From 2016 to 2017, he was a visiting researcher in Wireless Information Net-

work Laboratory (WINLAB), Rutgers University, United States. His current research interests include machine learning-based network control, machine learning in wireless networks, and heterogeneous resource management.



Masahiro Morikura received B.E., M.E. and Ph.D. degree in electronic engineering from Kyoto University, Kyoto, Japan in 1979, 1981 and 1991, respectively. He joined NTT in 1981, where he was engaged in the research and development of TDMA equipment for satellite communications. From 1988 to 1989, he was with the communications Research Centre, Canada as a guest scientist. From 1997 to 2002, he was active in standardization of the IEEE802.11a based wireless LAN. He received Paper Award, Achievement Award and Distinguished Achievement and Contributions Award from the IEICE in 2000, 2006 and 2019, respectively. He also received Education, Culture, Sports, Science and Technology Minister Award in 2007 and Maejima Award from the Teishin association in 2008 and the Medal of Honor with Purple Ribbon from Japan's Cabinet Office in 2015. Dr. Morikura is now a professor of the Graduate School of Informatics, Kyoto University. He is a Fellow of the IEICE and a member of IEEE.



Daisei Uchida received B.E. and M.E. degrees in applied physics from Tokyo Institute of Technology in 1994 and 1997, respectively. Since joining NTT Wireless Systems Laboratories in 1997, he has been engaged in R&D of the access scheme for satellite systems, radio channel assignment and tree topology of PHS-based local positioning and information systems to form wireless multi-hop networks autonomously, radio channel assignment and transmission power control for mesh-type broadband fixed wireless access systems, modulation-demodulation schemes for MIMO-OFDM systems, and modulation-demodulation schemes and radio circuit designs for Low Power Wide Area systems. He is currently engaged in R&D of distributed antennas systems using high frequency bands for 6G generation mobile technologies. He is a member of the Institute of Electronics, Information and Communication Engineers (IEICE) of Japan. He received the Young Engineers Award from IEICE in 2001.



Yushi Shirato received B.E., M.E and D.E. degrees in electrical engineering from Tokyo University of Science in 1990, 1992 and 2018, respectively. Since joining NTT Wireless Systems Laboratories in 1992, he has been engaged in R&D of adaptive equalizers, modems for fixed wireless access systems, and software defined radio systems. He is currently engaged in R&D of millimeter-wave-band very high throughput fixed wireless backhaul systems. He received the Best Paper Award in 2018 and the Young Engineer's Award in 2000 from IEICE, and the 18th Telecom

System Technology Award from the Telecommunications Advancement Foundation in 2003. He is a senior member of IEICE.



Naoki Kita received his B.E. degree from Tokyo Metropolitan Institute of Technology, Tokyo, Japan in 1994, and received his M.E. and Ph.D. degrees from Tokyo Institute of Technology, Tokyo, Japan in 1996 and 2007, respectively. Since joining NTT in 1996, he has been engaged in the research of propagation characteristics for wireless access systems, the development of future satellite communication systems, and international standardization on radio wave propagation. From 2009 to 2010, he was a visiting scholar at Stanford University, CA, USA. From

2013 to 2014, he was a visiting research scholar at Waseda University, Tokyo, Japan. He is currently a Senior Research Engineer, Supervisor, Group Leader at NTT Access Network Service Systems Laboratories, where he engages in the research and development of future wireless access network systems. He received the IEICE Young Researcher's Award, the IEICE Communications Society Best Paper Award, and IEICE Best Paper Award in 2002, 2010, and 2014, respectively. He also received the Best Paper Award in International Symposium on Antennas and Propagation 2016 (ISAP2016) in 2016. He is a senior member of IEICE and a member of IEEE.